Observation of strongly subhomogeneous linewidths using high-contrast transmission spectroscopy: Experiment and theory

Luo Caiyan, S. Kröll,* L. Sturesson, and S. Svanberg

Division of Atomic Physics, Lund Institute of Technology, P.O. Box 118, S-221 00 Lund, Sweden

(Received 24 August 1995)

Saturated absorption spectroscopy linewidths down to half the natural linewidth have been obtained for the sodium D_1 transition in a strongly absorbing gas cell. The strong-line-narrowing effect is achieved by using an experimental "tandem" approach with two absorbing cells in series, where the saturated absorption output from the first cell is used as an input beam for a saturated absorption measurement in the second cell. A physical interpretation of the line-narrowing mechanism in highly absorbing media is presented, which, among other things, explains why the narrowing effects are different for crossover transitions. It is further argued that in these experiments the line-narrowing effect is caused by optical pumping and can be appropriately described by rate equations. This is different from several other recent papers on high-contrast transmission spectroscopy, where full Bloch vector models were necessary to fully describe the line shapes. Here a rate equation model, which includes two spatial dimensions, is developed, and reasonable agreement is obtained between experimental and theoretical data.

PACS number(s): 32.80.Bx, 32.70.Jz, 32.90.+a

I. INTRODUCTION

Several papers have recently addressed the issue of obtaining subnatural linewidth and subnatural resolution by performing Doppler-free spectroscopy on samples of high optical density (so-called high-contrast transmission spectroscopy) [1–7]. In this paper we experimentally and theoretically demonstrate that lines with strongly subnatural linewidths can be obtained using high-contrast transmission spectroscopy (HCTS). Linewidths close to half the natural linewidth are obtained by using the so-called "tandem arrangement" [2] [standard and "tandem" experimental configurations are schematically shown in Figs. 1(a) and 1(b) respectively]. In the latter configuration the Doppler-free output signal from a saturation spectroscopy measurement on a high optical density cell is used as the input light source for a Doppler-free saturation spectroscopy measurement in a second cell, which also is of high optical density. Due to the line-narrowing effect of HCTS the Doppler-free output signal from this second cell may have a linewidth substantially lower than the natural linewidth.

The observed line narrowing is explained and supported by theoretical calculations. The theoretical modeling is based on rate equations specifically including velocity-selective optical pumping. Previous theoretical analyses have included rate equations [2,7] as well as optical Bloch equations [3–6]. The present experiment and calculations have been performed on the $3s\ ^2S_{1/2}-3p\ ^2P_{1/2}$ transition in sodium. We will briefly describe the prerequisites for the calculations. The coupling of the total angular momentum with the nuclear spin of $I=\frac{3}{2}$ turns this transition into a four-level system (neglecting the Zeeman degeneracy) with total angular momentum $F=1$ and $F=2$ in the upper as well as lower electronic state. The optically induced transparency is then

caused by velocity-selective optical pumping between the two ground-state hyperfine levels. At sample temperatures below 200 °C the mean free path of the sodium atoms is >1 m. This means that redistribution of optically hyperfine pumped atoms essentially then only occurs when the atoms collide with the walls of the cell and other collision processes can be neglected. An atomic velocity of 600 m/s perpendicular to the laser beam and a 2-mm-diameter beam yields a transit time through the beam for the atoms of about 3 μs. This consequently would more or less be the average time until an optically pumped atom is replaced by an unpumped atom. With an upper state lifetime of 16 ns the transit time through the beam is much longer than any coherence between the ground and excited state. Although use of the
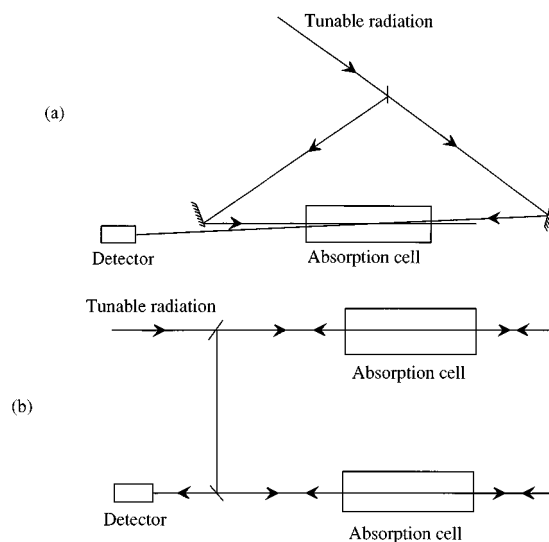

FIG. 1. (a) Schematic view of the optical layout of a conventional Doppler-free saturated absorption spectroscopy setup. (b) Schematic view of the optical layout of a Doppler-free high-contrast tandem spectroscopy setup.

---

*FAX: +46-46 222 42 50.

Block equations is required to give a complete description of the physics involved in the excitation, similar arguments have been used previously for justifying the use of rate equations for modeling certain aspects of Doppler-free saturation-type experiments [8]. The novelty of the present approach is the treatment of spatial effects on the transmitted laser beam due to the optical pumping. The outer parts of the counterpropagating laser beams exhibit a larger absorption since they see atoms that have not been pumped while in the center of the beam, most atoms have already been pumped to an inactive nonabsorbing state. An effect not accounted for in the present calculations is that the optical fields may introduce a long-lived coherence between the magnetic sublevels within one of the ground-state hyperfine levels [9,10] in a manner similar to that investigated, e.g., by Suter and co-workers [11,12]. This ground-state coherence is discussed in a related paper [9], but has been neglected here. In addition, third-order effects such as self-focusing and defocusing have been neglected.

The layout of the paper is as follows; in the next section the theoretical model is described. In Sec. III the experimental setup is described together with some experimental data. Experimental and theoretical data are compared in Sec. IV and a physical interpretation of the results is given and, finally, in Sec. V, the main results of the investigation are summarized.

II. THEORY

The subnatural line-narrowing effect is computed by calculating the frequency-dependent beam absorption through the frequency-dependent absorption coefficient. The absorption coefficient is obtained from the frequency-dependent upper and lower state population, which are calculated using a rate equation approach. Saturation spectroscopy is commonly described by the hole-burning model. In an experiment where the atom interacts with the light during a period that is long in comparison to the relaxation time of the off-diagonal density matrix elements, the interaction can be appropriately described using rate equations. In a rate equation description of saturation spectroscopy, spatial variations of the state population densities are often not taken into account. Commonly, the theoretical description of saturation spectroscopy has been one dimensional; i.e., only the population and the intensity along the direction of propagation have been considered. However, for high-contrast transmission spectroscopy, spatial variations have a pronounced effect on the transmitted beams, since the optical pumping preferably occurs shortly after the atoms have entered the beam. Thus, the center of the probe beam may see a transparent sample while the outer part of the beam is strongly absorbed. To model the subnatural narrowing of high-contrast transmission spectroscopy we have therefore adopted a procedure where both the radial and axial dependence of the laser-beam intensity and the population distribution are explicitly taken into account. In describing the model we will begin with a one-dimensional three-level system and gradually extend the description to a full two-dimensional multilevel system. First consider three-level atoms with one excited state, one ground state, and some reservoir state to which excited atoms may relax. The time

development of the fractional number density of excited state atoms, n_e, interacting with two counterpropagating laser beams coupling ground and excited state is given by

$$\dot{n}_e = (n_g - n_e)(\sigma_+ F_+ + \sigma_- F_-) - \frac{n_e}{\tau} + (n_e^0 - n_e)\frac{1}{T},$$
(1a)

with a similar equation for the ground-state number density, n_g,

$$\dot{n}_g = -(n_g - n_e)(\sigma_+ F_+ + \sigma_- F_-) + A_{ge}n_e + (n_g^0 - n_g)\frac{1}{T}.$$
(1b)

The first term on the right-hand side in Eq. (1a) describes optical pumping. The $+$ and $-$ indices indicate the different propagation directions of the laser beams. F is the laser photon flux [photons/(area×time)], σ is the absorption cross section. The second term in Eq. (1a) corresponds to spontaneous decay, τ is the lifetime of the excited state, and the last term describes the effect of atoms physically entering and leaving the volume irradiated by the laser beam. T is the transit time, i.e., the average time it takes the atoms to travel through the laser beam, the 0 superscript indicates the unpumped population density outside the laser beams due to the Boltzmann distribution and in Eq. (1b) A_{ge} represents the transition probability from state e to state g. Due to the hole burning the number densities are different for different atomic velocity groups. The number densities are also functions of the laser frequency, $\omega = 2\pi v$ and of the position along the laser beam.

For the continuous-wave case the equations are plainly solved at steady-state conditions. To calculate the transmission of the laser beam, the sample is divided into length elements along the laser beam (z axis). The absorption coefficient the laser beam experiences in, e.g., the $+$ direction in one of these length elements at frequency ω, is then calculated as

$$\alpha_+(\omega) = \int_{v_z} [n_g(\omega, v_z) - n_e(\omega, v_z)]\sigma_+(\omega, v_z)f(v_z)dv_z.$$
(2)

Here $f(v_z)$ is the Maxwellian velocity distribution and v_z is the projected velocity along the laser beams. Performing calculations around the line center this distribution could be approximated with a constant. The transmitted intensity for, e.g., the pump beam, through each length element of length Δz becomes

$$I_+(\omega, n) = I_+(\omega, n-1)e^{-\alpha_+(\omega)\Delta z}.$$
(3)

To expand the model into two dimensions each length element was divided into radial shells. As the laser beam is propagating through the cell its transverse intensity distribution changes. The intensity of the outer parts of the laser beam have generally seen unpumped atoms and have experienced a strong absorption while the inner parts may have encountered only atoms pumped into a noninteracting state and thus have not experienced any significant absorption. It turns out that this effect calls for a model that handles the

originally rather large contributions of optical pumping in the outer parts of the beam and still has a high degree of spatial resolution in the central parts of the beam. Therefore, the thickness of the radial shells has been chosen to be larger for shells with large radius than for shells with smaller radius. This is shown in Fig. 2. The innermost shell, i.e., the center of the laser beam, is designated by the number 0. The atoms that enter the radial shell number i, for the first time, come from the next outer shell, $i+1$, and are moving inwards. Depending on their trajectories, a fraction of them will not go on into the next, inner, shell $(i-1)$. Instead they will return to the $i+1$ shell and then consecutively pass to shells number $i+2$, $i+3$, etc. We define atoms that already have reached their closest point to the laser beam center as outward moving atoms. The distinction between inward and outward moving atoms is necessary because the fraction of unpumped atoms will generally not be the same for these two groups of atoms.

The intensity in the central part of a laser beam (TEM$_{00}$ single frequency) is always higher than in the outer part of the beam. The incoming laser beam is assumed to exhibit a Gaussian intensity distribution. The maximum transit time for atoms going through the center of the beam has been chosen to be 200 times the natural lifetime of the excited state in the calculations in order to model the experimental conditions. With a 16-ns lifetime and a velocity of 600 m/s this means that the laser beam diameter is chosen such that $>99\%$ of the laser intensity resides within a radius of about 2.7 mm.

As the experimental signals primarily exhibiting anomalous line narrowing are the crossover signals, we extended the model to a true four-level system, with two ground states and two excited states, like the D_1 line of sodium. Although there are only four levels involved in a crossover transition, the state population is different for the atoms moving towards and away from the laser beam center. Therefore eight rate equations are needed in order to describe the optical pumping behavior. Two of these are shown below; one for atoms in excited state 1, moving towards the laser beam
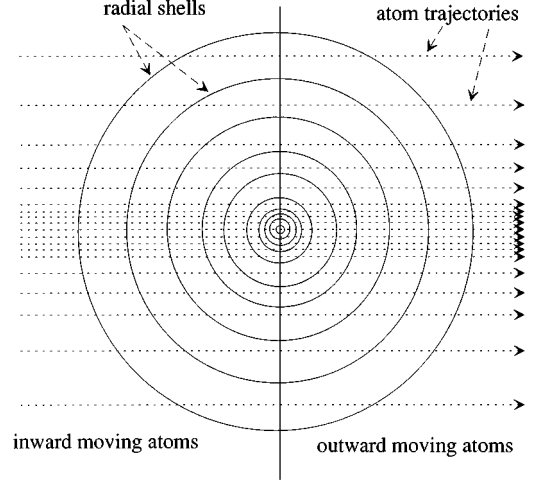

FIG. 2. For the calculations each length section of the laser beam is divided into radial shells of different thickness. Some of all the possible (straight line) trajectories for atoms passing through the laser beam are shown. The atoms move along the trajectories from the left to the right in the picture. The laser beam is propagating perpendicular to the plane of the paper. The relative size of the different radial shells is shown in the figure. Depending on whether the atoms have reached their point of closest approach to the laser beam center or not, the atoms are characterized as inward or outward moving. The innermost shell is numbered zero and the numbering increases outwards in consecutive order. Outward-moving atoms will always go from shell number i to shell number $i+1$, inwards moving atoms will always go from shell number i to shell number $i-1$ until they change from being inward moving to being outward moving. This change takes place when they cross the vertical line through the laser beam center. As can be seen this can happen in any shell. This is explicitly taken into account in the calculations.

center and one for atoms in ground-state level 2 moving away from the laser beam center. For completeness, all eight equations are given in the Appendix.

$$\dot{n}_{e1}^{\text{in}}(i,\omega,v_z,n)=[n_{g1}^{\text{in}}(i,\omega,v_z,n)-n_{e1}^{\text{in}}(i,\omega,v_z,n)]\frac{1}{6}\left(\sigma_{11+}(\omega,v_z)\frac{I_+(i,\omega,n)}{\hbar\omega}+\sigma_{11-}(\omega,v_z)\frac{I_-(i,\omega,n+1)}{\hbar\omega}\right)$$

$$+\left(\frac{3}{5}n_{g2}^{\text{in}}(i,\omega,v_z,n)-n_{e1}^{\text{in}}(i,\omega,v_z,n)\right)\frac{5}{6}\left(\sigma_{21+}(\omega,v_z)\frac{I_+(i,\omega,n)}{\hbar\omega}+\sigma_{21-}(\omega,v_z)\frac{I_-(i,\omega,n+1)}{\hbar\omega}\right)$$

$$-\frac{n_{e1}^{\text{in}}(i,\omega,v_z,n)}{\tau}+[n_{e1}^{\text{in}}(i+1,\omega,v_z,n)-n_{e1}^{\text{in}}(i,\omega,v_z,n)]\frac{1}{T(i)}, \tag{4a}$$

$$\dot{n}_{g2}^{\text{out}}(i,\omega,v_z,n)=-\left(n_{g2}^{\text{out}}(i,\omega,v_z,n)-\frac{3}{5}n_{e1}^{\text{out}}(i,\omega,v_z,n)\right)\frac{1}{2}\left(\sigma_{21+}(\omega,v_z)\frac{I_+(i,\omega,n)}{\hbar\omega}+\sigma_{21-}(\omega,v_z)\frac{I_-(i,\omega,n+1)}{\hbar\omega}\right)$$

$$-[n_{g2}^{\text{out}}(i,\omega,v_z,n)-n_{e2}^{\text{out}}(i,\omega,v_z,n)]\frac{1}{2}\left(\sigma_{22+}(\omega,v_z)\frac{I_+(i,\omega,n)}{\hbar\omega}+\sigma_{22-}(\omega,v_z)\frac{I_-(i,\omega,n+1)}{\hbar\omega}\right)$$

$$+A_{21}n_{e1}^{\text{out}}(i,\omega,v_z,n)+A_{22}n_{e2}^{\text{out}}(i,\omega,v_z,n)+\{[1-\theta(i)]n_{g2}^{\text{out}}(i-1,\omega,v_z,n)+\theta(i)n_{g2}^{\text{in}}(i,\omega,v_z,n)$$

$$-n_{g2}^{\text{out}}(i,\omega,v_z,n)\}\frac{1}{T(i)}. \tag{4b}$$

TABLE I. Definition of the parameters in Eqs. (4a) and (4b) and in the Appendix.

Parameter	Definition
n_{ek}	Density of atoms in excited state k ($k=1$ or $k=2$)
n_{gl}	Density of atoms in ground state l ($l=1$ or $l=2$)
n_{ek}^0	Density of atoms in excited state k outside the laser beam (n_{ek}^0 is assumed to be zero)
n_{gl}^0	Density of atoms in ground state l outside the laser beam
$\sigma_{lk\pm}$	Cross section for $I_\pm$ and the transition between the lth ground state and the kth excited state
A_{ge}	Transition probability between excited state e and ground state g
$A_{11}=1/6\tau$	
$A_{12}=1/2\tau$	
$A_{21}=5/6\tau$	
$A_{22}=1/2\tau$	
n	Index describing the length position in the cell, along the z axis
$T(i) \propto [r^2(i)-r^2(i-1)]/r_i$	Mean transit time through shell i
$r(i)$	Radius of shell i, $i=0,...,9$
$\theta(i)=[r(i)-r(i-1)]/r(i)$	Fraction of atoms in shell i transferring from in- to out-moving group

Symbols and notation are explained in Table I. The upper index indicates inward and outward moving atoms, respectively. The explicit notation of the dependence of the parameters i, ω, v_z, and n will be dropped further on in order to save space. The principal relations are the same as in the simple two-level model described earlier.

The equations describe the change in atomic density for each state and for each shell (i) for atoms traveling towards and from the laser beam center. The first two terms of either right-hand expression describe optical pumping. I_+ or I_- is the intensity of the respective laser beam, $\hbar\omega$ is the photon energy and σ is the cross section. Further definitions are given in the Appendix. The next term(s) describes the influence of spontaneous decay. τ is the lifetime of the excited state and A_{lk} is the transition probability between the lth ground state and the kth excited state. The last term in either equation describes the effect of atoms physically entering and leaving the laser beam. In the case of the outwards moving atoms there is an input flow both from the inner shell and from atoms in the same shell that never went into the inner shell. From pure geometrical considerations the relative size of these contributions is given by the ratio $[r(i)-r(i-1)]/r(i-1)$. These source terms are expressed in terms of $\theta(i)$, the fraction of atoms in shell i changing from moving inward, towards the beam center, to moving outward. For the innermost shell the transfer term, $\theta(0)$, is equal to 1. $T(i)$ is the transit time, i.e., the time the atom spends inside shell i in the laser beam.

For $i=9$ the expressions $n_{ek}^{\text{in}}(i+1,\omega,v_z,n)$ and $n_{gl}^{\text{in}}(i+1,\omega,v_z,n)$ in the equations above are substituted with n_{ek}^0 and n_{gl}^0, respectively, where $n_{ek}^0=0$. The upper 0 index indicates the population of either state at zero light intensity due to the Boltzmann distribution. Indices e and g indicate the excited and ground states, respectively, and indices k and l can take values 1 and 2 corresponding to hyperfine quantum numbers $F=1$ and $F=2$.

The cell is divided into a number of separate slices along the beam direction, typically 40 or 80. The calculations start by letting the laser input beam, which has a Gaussian intensity profile, propagate into the first slice. (In this first iteration the beam propagating in opposite direction is assumed to be zero, at this time we therefore have only one beam propagating in a single direction through the cell.) Each slice is in turn divided into ten radial shells and for each of these shells there are eight equations as Eq. (4). In total the population transfer in this slice is therefore described by 80 coupled first-order differential equations. This equation system is solved in steady state using the CERN library computer routine DEQN. The population distribution within a group of atoms moving at a specific velocity, v_z, along the laser beam propagation direction is then obtained. In total, the inhomogeneous line profile has been divided into 96 such velocity groups. By solving the system of 80 coupled equations for each of the 96 velocity groups, the frequency-dependent absorption coefficient α can be calculated for each shell, i, as

$$\alpha(i) = \int_{v_z} (n_{g1}-n_{e1}) \frac{1}{6} \sigma_{11+}f_{11}\,dv_z$$

$$+ \int_{v_z} \left(n_{g1}-\frac{3}{5}n_{e2}\right) \frac{5}{6} \sigma_{12+}f_{12}\,dv_z$$

$$+ \int_{v_z} \left(n_{g2}-\frac{5}{3}n_{e1}\right) \frac{1}{2} \sigma_{21+}f_{21}\,dv_z$$

$$+ \int_{v_z} (n_{g2}-n_{e2}) \frac{1}{2} \sigma_{22+}f_{22}\,dv_z. \qquad (5)$$

Here we use the average of the in-moving and out-moving atoms:

$$n_{gl}(i,\omega,v,n) = n_{gl}^{\text{in}}(i,\omega,v,n) + n_{gl}^{\text{out}}(i,\omega,v,n), \quad \text{etc.} \quad (6)$$

and have introduced $f_{lk} = f_{lk}(v_z)$ =the relative number of atoms moving with a certain velocity within a Maxwellian distribution. The cross section of the transition between the first ground state and the first excited state has the following expression:

$$\sigma_{11+} = \frac{\sigma_0}{1 + \{[\nu_0 + \nu_g/2 - \nu_e/2 - (\nu - \nu_0 v_z/c)]/(\Delta\nu_N/2)\}^2} \cdot \quad (7)$$

σ_0 is the cross section at resonance, $\Delta\nu_N$=natural linewidth [full width at half maximum (FWHM)], ν_0=resonance frequency, ν_g is the splitting of the ground state, ν_e is the splitting of the excited state, c is the speed of light. The transmitted intensity from one slice to the other is then readily calculated using Eq. (3). This procedure is performed consecutively for all slices to the end of the cell. The transmitted intensity is multiplied by the reflection coefficient (70% to include losses in windows, etc.) and the reflected light propagating in the opposite direction is now the input to the last slice. In this calculation the beam propagating in the opposite direction is nonzero. (It has the value just calculated for the light propagating in the opposite direction before the reflection.) The iteration proceeds all through the cell and an output intensity from the two-way passage through the cell is obtained. A new calculation, the second iteration, is now performed from the start of the cell with the difference that the counterpropagating beam has a nonzero value already in the first slice. It has the value that was just calculated in the first iteration. This calculation back and forth through the cell is repeated k times until the convergence criterion defined as

$$\sum_{\substack{\text{number} \\ \text{of shells}}} \left(\frac{I_{\text{out}}^i(k) - I_{\text{out}}^i(k-1)}{I_{\text{out}}^i(k)} \right)^2 < (\text{number of shells}) \times 10^{-6}$$
$$(8)$$

is met, where I_{out}^i is the output intensity from the shell i. (Number of shells is normally 10 but can be less as described below.) At this point the output intensity has been calculated for a specific laser frequency. This process is then repeated for additional frequencies. The frequency separation between the different points is typically $\frac{1}{8}$ FWHM. The output from the first cell is then sent into the second cell. In most of the runs the cells were divided into either 40 slices or into 80 slices in the case of strong beams, as for the primary cell case. In order to save computer CPU time, shells where the light intensity was less than 10^{-6} of the saturation intensity were excluded. This simplification mainly affects the calculations of the secondary cell, since in the first cell the intensity is still high in most shells.

III. EXPERIMENT

The experimental setup for the tandem arrangement is shown in Fig. 3. The two sodium cells are made of Pyrex. They are 30 cm long and have a diameter of 25 mm. They were supplied with sodium by distillation after several hours of bakeout at high temperatures while connected to a high-vacuum bench. The sodium cells are put into copper tubes, which are electrically heated. The temperature of each cell is
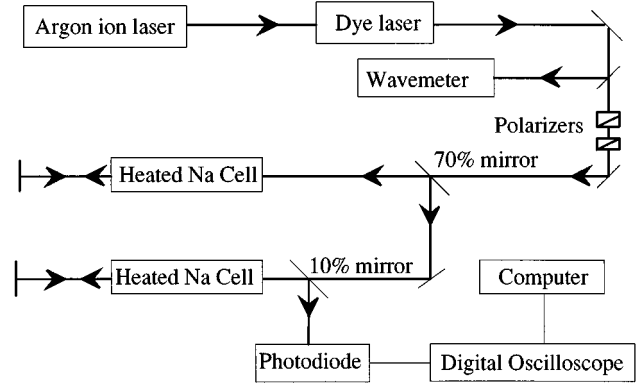

FIG. 3. Experimental setup.

monitored with two digital thermometers, one thermometer is used to monitor the temperature close to the middle of the cell and the other is used to monitor the temperature close to a cell window. In order to prevent sodium from condensing on the windows turning them into mirrors it is important that the cell windows are not the coldest part of the cell. In our experiments, the coldest temperature is below 200 °C.

The laser system consists of a Coherent CR 699-21 ring dye laser with a nominal line width of 1 MHz, which is pumped by a Coherent CR-12 argon ion laser. Typically the input beam at the first cell had a 2-mm diameter and a power of 300 mW. The characteristics of the beam splitters were chosen as described below. The output signal after the double passage through the second cell is recorded by a photodiode connected to a Tektronics 2431L digital storage oscilloscope.

Figure 4 shows the hyperfine structures of the D_1 line of sodium recorded using conventional saturation spectroscopy [with a setup of the kind shown in Fig. 1(a)] and as an inset the energy-level diagram is shown. Letters have been assigned to each of the Doppler-free signals for future reference in the paper. Mainly the line narrowing of transitions a, b, and c was investigated and the strongest narrowing effect was observed for the crossover transition designated b. This will be further discussed in Sec. IV. For experiments using only a single sodium cell the narrowest linewidth observed was of the order of the natural linewidth for the experimental conditions chosen in these studies (subnatural linewidths were demonstrated for the single-cell case in Ref. [2]). In the tandem experiments, the nonlinear frequency-dependent output signal from the first sodium cell is used as the input of the second cell. This procedure significantly enhances the line-narrowing effect [2]. Experimentally it is important to match the input intensity and the optical density of the cells to obtain maximum line-narrowing effect. A high optical density will enhance the narrowing effect [2]; this requires a high input intensity in order to have at least some transmission through the cell. However, at the output of the second cell the light must be smaller than the saturation intensity in order to obtain a narrowing effect. Two polarizers are therefore used to control the laser intensity such that the line-narrowing effect could be maximized. To achieve a good contrast ratio between excitation on and off the Doppler-free lines, spatial filters are used to eliminate scattering light. Figure 5 shows a recording where the crossover linewidth is 5.5
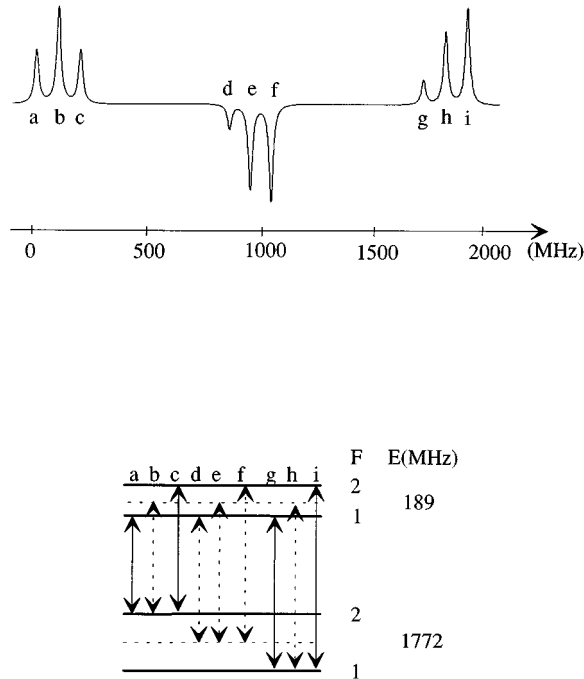
FIG. 4. Doppler-free saturation spectroscopy recording of the sodium D_1 line at 589 nm. As an inset the energy-level diagram where the hyperfine transitions and the crossover lines have been indicated is included. Total angular momentum, F, and energy-level splitting, E, have been given in the diagram.

MHz. This is close to half the natural linewidth of 9.7 MHz. The temperature of the first cell was 172 °C and the second cell temperature was 157 °C for this recording.

IV. DISCUSSION OF RESULTS

For a general understanding of the line narrowing it may be helpful to consider Fig. 6. This figure schematically shows the velocity distribution of the ground-state atoms projected on the propagation direction of the laser probe and pump beams as well as the Bennett holes [13] burnt into this profile by the pump and probe laser beams for the sodium atom four-level D_1 line. Lower case italic letters refer to Bennett holes burnt by the probe beam and upper case italic
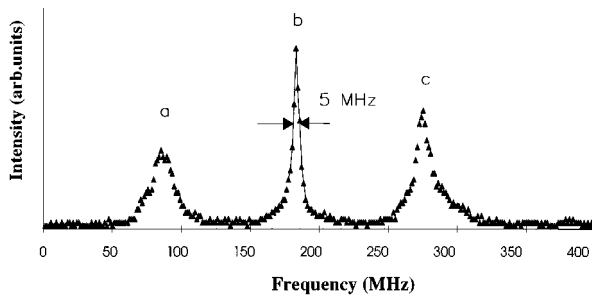

FIG. 5. Experimental recording of a selected part of the sodium D_1 line. From left to right the $F_l = 2 \rightarrow F_u = 1$ transition, the $F_{1l} = 2 \rightarrow F_u = 1,2$ crossover and the $F_l = 2 \rightarrow F_u = 2$ line are shown (F_l and F_u are upper and lower state angular momentum, respectively). The crossover linewidth is 5 MHz, which is about 50% of the 10-MHz natural linewidth. The other two lines are about 20 MHz broad.
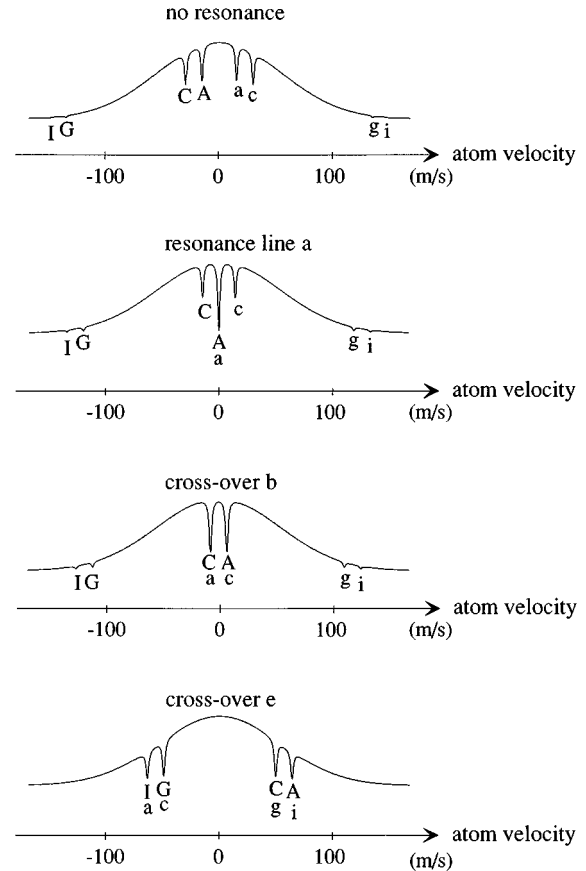

FIG. 6. Velocity profiles showing the Bennett holes from two counterpropagating narrow-band laser beams for the ground-state absorption profile when the laser is tuned to various transitions. The description of the resonances, resonance a and crossovers b and e refer to the lettering in Fig. 4. Upper and lower case letters refer to Bennett holes created by the pump and probe beam, respectively. Also these letters refer to the corresponding transition in Fig. 4.

letters refer to those burnt by the pump beam. As the laser is tuned to the Doppler-free resonances, the Bennett holes burnt by the different beams overlap. The leftmost resonance in Fig. 4 occurs when the Bennett holes a and A overlap in Fig. 6. At this laser frequency, atoms in seven different velocity groups absorb the laser radiation. One velocity group is shared by both pump and probe beam. When the laser is detuned from the Doppler-free resonances there are, as can be seen in the top trace in Fig. 6, eight absorbing velocity groups. Consequently, the light absorption is lower at the Doppler-free lines. For the upper and lower state crossovers, lines b and h in Fig. 4, Bennett holes a and C and c and A, and, g and I and i and G, respectively, overlap. For both these cases there are only six absorbing velocity groups. Here the laser beam absorption, consequently, is even less than for lines a, c, g, and i. For line e, four Bennett holes overlap (a and I, c and G, g and C, and i and A.). However, while the probe laser tries to drive atoms in velocity group a from the $F = 2$ ground state to the $F = 1$ ground state, the pump beam tries to drive the same velocity group from the $F = 1$ to the $F = 2$ state. Thus, an atom pumped by one beam will now be available for absorbing photons from the other
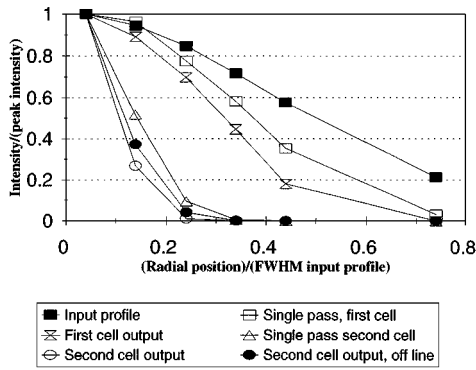
FIG. 7. The laser beam intensity, normalized to unity at the laser beam center, versus radial distance from laser beam center after each passage through the absorption cells (the distance from the laser beam center is expressed in terms of full widths at half maximum of the input beam profile). The laser frequency is tuned to the upper state crossover, but the spatial profile for the final output after the second cell is also shown when the laser is tuned within the Doppler-broadened resonance line but not to any Doppler-free resonance (black ellipses). The lines between markers only serve as guide for the eye. For further comments see text.

FIG. 8. Recorded linewidth for the $F_l=2 \rightarrow F_u=1,2$ crossover in terms of the natural linewidth as a function of the absorption ($\alpha L = \ln$ [(second cell input intensity)/(transmitted intensity)]) in the second cell. Some data for the experiment are given in Table II. The data indicate that both the experimental and the theoretically calculated linewidths decrease towards the same asymptotic value as the optical density increases. The theoretical calculations, however, are more sensitive to changes in the cell absorption.

beam. Although there are now in total only four absorbing velocity groups, no atoms can be pumped into an inactive state. Consequently, the absorption will be particularly strong for line e (and to a somewhat lesser extent also for lines d and f, where a similar situation applies) as can be seen in Fig. 4.

From the discussion above we can conclude that in cases like the sodium D_1 line where there are several absorbing transitions within the inhomogeneous Doppler profile, a single pump beam frequency is not sufficient to make the sample completely transparent to the probe beam. This is because there are several absorbing velocity groups and they can, at least not in the general case, all be pumped simultaneously by a beam with the same frequency propagating in opposite direction. It is also clear that on the true resonances and, even more so, on the upper-state crossover transitions, an optical pumping effect making the sample transparent for the probe beam indeed occurs. In consistence with this it also experimentally turns out that the subnatural line-narrowing effect indeed is the strongest for the upper-state crossover lines. Both theoretically and experimentally it is also clear that the spatial profile of the transmitted probe beam is different for different hyperfine components. The transmission of the central parts of the probe beam is determined by how effective the outer part of the pump and probe beams have been in pumping the atoms into a nonabsorbing level. Experimentally, using a charge coupled device array beam profile detector, this was most evident when comparing the spatial structure of the transmitted beam when the laser was tuned to the upper-state crossover denoted b in Fig. 4 and the level crossover denoted e in Fig. 4. Not only the frequency distribution of the transmitted beam was narrower for the upper-state crossover but also the spatial profile was narrower. This is also verified by the theoretical calculations. Figure 7 shows the laser beam intensity, normalized to unity at the beam center, versus radial distance when the laser frequency is tuned to the upper-state crossover. Solid squares represent the input profile when the beam enters the first cell,
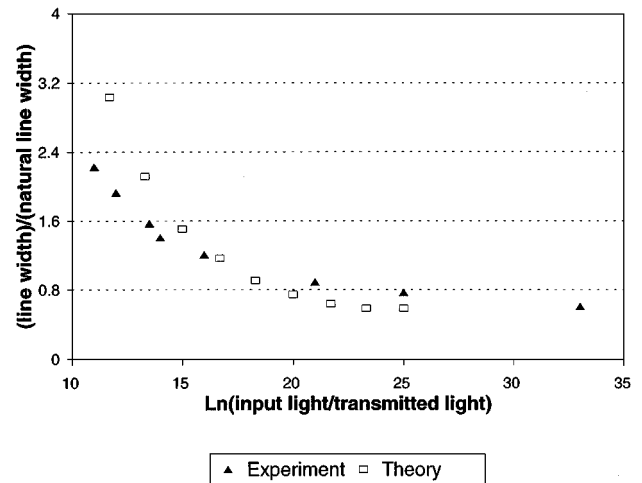
open squares represent the profile after a single pass through the first absorption cell, i.e., at the retroreflecting 100% mirror behind the cell (compare Fig. 3). Hour glasses show the profile at the first cell output, i.e., this is also the profile when the beam enters the second cell, triangles show the profile after a single passage through the second cell and open ellipses correspond to the output from the second cell. Black ellipses show the profile after the second cell when the laser is tuned within the Doppler-broadened resonance line but not exactly to a Doppler-free resonance. As can be seen the profile is slightly more narrow at the crossover line. The theoretical calculations also show that the intensity of the output beam tuned to the crossover line (open ellipses) is much higher, about five orders of magnitude (this is not shown in the figure), than for the beam that is not tuned to a Doppler-free resonance (black ellipses). Clearly, the reason for this is that when the laser frequency is tuned to the crossover resonance, the returning laser beam after the single passage through each cell only encounters atoms that have been pumped into a nonabsorbing state, while off the Doppler-free resonance returning beams experience the same absorption as during the first single pass. As can be seen in Fig. 7 the spatial narrowing during the propagation is quite significant.

Figure 8 shows the experimental and theoretical linewidth in units of the natural linewidth for the upper-state crossover as a function of sodium atom concentration in the second cell. The experimental conditions at a linewidth of 6 MHz are given in Table II. The sodium atom density, N, versus cell temperature, T, is obtained using the experimental data determined in Ref. [14]. The quantity αL is referred to as the absorption below. [$\alpha L = N(T)\sigma L$ where L is the cell length, σ the absorption cross section at zero light intensity, and α is the absorption coefficient]. The theoretical calculations are able to predict the experimentally observed line-narrowing effect, without any adjustable parameters. However, for the

TABLE II. Experimental parameters at a line width of 6 MHz (close to one-half of the natural linewidth).

Parameter	Value
Peak laser intensity (mW/mm^2)	50
Laser beam diameter (mm)	2
First cell absorption αL	60
Second cell absorption αL	33
Fraction transmitted intensity (after second cell)	10^{-3}

intensity used in the experiments the theoretical model predicts a too high optical density for the value when the line narrowing starts and a too low laser light transmission through the cells. The reason for this can be third-order nonlinear effects leading to self-focusing and defocusing [15] or, laser-induced ground-state coherence, neither of which have been included in the theoretical treatment. Since the present experiment is carried out on the low-frequency side of the absorption line, self-defocusing will occur [15]. Effectively this will have the effect that the actual intensity in the cell will be lower than expected. It is therefore qualitatively correct that the input intensity in the theoretically calculated case must be lower than in the experimental case to obtain agreement between experimental and theoretical values. (In consistence with this the theoretical intensity was reduced by an extra factor when the light was propagating from cell one to cell two. To obtain agreement the extra reduction had to be a factor of four, which may seem a bit high. On the other hand the input intensity at cell one was slightly higher in the theoretical calculations than in the experiment.) Self-defocusing does, however, not explain why the difference in transmitted intensity between the theoretical and experimental cases are so large. As a general comment the transmitted intensity is very strongly dependent on the input intensity. Overall it is noticed that the conditions at which the theoretical calculations reproduce the experimentally observed narrowing, the theoretical value for the transmission is much too small. We do not know the reason for this. The line narrowing is also more sensitive to changes in the absorption in the theoretical calculations than in the experiment as can be seen in Fig. 8. Nevertheless, the fact that the theoretical model is able to predict the general linewidth behavior and that it converges at the experimentally observed lowest value of 0.55 times the natural linewidth makes it reasonable to believe that optical pumping in combination with spatial effects

can be a major cause of the subnatural line narrowing. This is an important aspect considering the various analyses that have been performed concerning high-contrast transmission spectroscopy [1–7]. The present analysis rather complements than contradicts or corrects the existing analyses. It treats the little discussed influence of optical pumping in high-contrast transmission spectroscopy, that may be the in practice most commonly encountered case.

V. SUMMARY AND CONCLUSIONS

Using high-contrast transmission saturation spectroscopy in the so-called tandem setup, with two high optical density absorption cells in series, saturated absorption linewidths down to half the natural linewidth have been obtained for the sodium D_1 transition. Several papers have recently discussed theoretical approaches to describe the subnatural line-narrowing effect in high-contrast transmission spectroscopy. Here we show that optical pumping including two spatial dimensions can be used to describe the effect. We note that the spatial profile of the transmitted beam in high contrast transmission spectroscopy is different for different types of Doppler-free transitions and, finally, an intuitive physical presentation of why the subnatural line-narrowing effect is different for different types of saturated absorption lines has also been given.

APPENDIX

For completeness all eight equations describing the spatially resolved optical pumping are given below. Two of these were given in Eqs. (4a) and (4b). As before symbols and notation are explained in Table I. The upper indices, in and out, represent atoms moving towards and away from their point of closest approach to the laser beam center, respectively. The numerical factors $\frac{1}{6}$, $\frac{1}{2}$, $\frac{3}{5}$, and $\frac{5}{6}$ need to be present since the intensity ratio between the different components $F=1\rightarrow F=1$, $F=1\rightarrow F=2$, $F=2\rightarrow F=1$, $F=2\rightarrow F=2$ for a Russell-Saunder type coupling case are (in arbitrary units) $\frac{1}{2}$, $\frac{5}{2}$, $\frac{5}{2}$, and $\frac{5}{2}$, respectively [16], and the fact that the relative number atoms in states $F=1$ and $F=2$ proportional to $2F+1$. Thus the transition probability per atom for the four transitions above will be $\frac{1}{6}$, $\frac{5}{6}$, $\frac{1}{2}$, and $\frac{1}{2}$, respectively.

$$\dot{n}_{e1}^{\text{in}}(i,\omega,v_z,n)=[n_{g1}^{\text{in}}(i,\omega,v_z,n)-n_{e1}^{\text{in}}(i,\omega,v_z,n)]\frac{1}{6}\left(\sigma_{11+}(\omega,v_z)\frac{I_+(i,\omega,n)}{\hbar\omega}+\sigma_{11-}(\omega,v_z)\frac{I_-(i,\omega,n+1)}{\hbar\omega}\right)$$

$$+\left(\frac{3}{5}n_{g2}^{\text{in}}(i,\omega,v_z,n)-n_{e1}^{\text{in}}(i,\omega,v_z,n)\right)\frac{5}{6}\left(\sigma_{21+}(\omega,v_z)\frac{I_+(i,\omega,n)}{\hbar\omega}+\sigma_{21-}(\omega,v_z)\frac{I_-(i,\omega,n+1)}{\hbar\omega}\right)$$

$$-\frac{n_{e1}^{\text{in}}(i,\omega,v_z,n)}{\tau}+[n_{e1}^{\text{in}}(i+1,\omega,v_z,n)-n_{e1}^{\text{in}}(i,\omega,v_z,n)]\frac{1}{T(i)},\tag{A1a}$$

$$\dot{n}_{e2}^{\text{in}}(i,\omega,v_z,n)=\left(\frac{5}{3}\,n_{g1}^{\text{in}}(i,\omega,v_z,n)-n_{e2}^{\text{in}}(i,\omega,v_z,n)\right)\frac{1}{2}\left(\sigma_{12+}(\omega,v_z)\,\frac{I_+(i,\omega,n)}{\hbar\omega}+\sigma_{12-}(\omega,v_z)\,\frac{I_-(i,\omega,n+1)}{\hbar\omega}\right)$$

$$+\left[n_{e2}^{\text{in}}(i,\omega,v_z,n)-n_{ek}^{\text{in}}(i,\omega,v_z,n)\right]\frac{1}{2}\left(\sigma_{22+}(\omega,v_z)\,\frac{I_+(i,\omega,n)}{\hbar\omega}+\sigma_{22-}(\omega,v_z)\,\frac{I_-(i,\omega,n+1)}{\hbar\omega}\right)$$

$$-\frac{n_{e2}^{\text{in}}(i,\omega,v_z,n)}{\tau}+\left[n_{e2}^{\text{in}}(i+1,\omega,v_z,n)-n_{e2}^{\text{in}}(i,\omega,v_z,n)\right]\frac{1}{T(i)},\tag{A1b}$$

$$\dot{n}_{e1}^{\text{out}}(i,\omega,v_z,n)=\left[n_{g1}^{\text{out}}(i,\omega,v_z,n)-n_{e1}^{\text{out}}(i,\omega,v_z,n)\right]\frac{1}{6}\left(\sigma_{11+}(\omega,v_z)\,\frac{I_+(i,\omega,n)}{\hbar\omega}+\sigma_{11-}(\omega,v_z)\,\frac{I_-(i,\omega,n+1)}{\hbar\omega}\right)$$

$$+\left(\frac{3}{5}\,n_{g2}^{\text{out}}(i,\omega,v_z,n)-n_{e1}^{\text{out}}(i,\omega,v_z,n)\right)\frac{5}{6}\left(\sigma_{21+}(\omega,v_z)\,\frac{I_+(i,\omega,n)}{\hbar\omega}+\sigma_{21-}(\omega,v_z)\,\frac{I_-(i,\omega,n+1)}{\hbar\omega}\right)$$

$$-\frac{n_{e1}^{\text{out}}(i,\omega,v_z,n)}{\tau}+\{[1-\theta(i)]n_{e1}^{\text{out}}(i-1,\omega,v_z,n)+\theta(i)n_{e1}^{\text{in}}(i,\omega,v_z,n)-n_{e1}^{\text{out}}(i,\omega,v_z,n)\}\frac{1}{T(i)},\tag{A1c}$$

$$\dot{n}_{e2}^{\text{out}}(i,\omega,v_z,n)=\left(\frac{5}{3}\,n_{g1}^{\text{out}}(i,\omega,v_z,n)-n_{e2}^{\text{out}}(i,\omega,v_z,n)\right)\frac{1}{2}\left(\sigma_{12+}(\omega,v_z)\,\frac{I_+(i,\omega,n)}{\hbar\omega}+\sigma_{12-}(\omega,v_z)\,\frac{I_-(i,\omega,n+1)}{\hbar\omega}\right)$$

$$+\left[n_{g2}^{\text{out}}(i,\omega,v_z,n)-n_{e2}^{\text{out}}(i,\omega,v_z,n)\right]\frac{1}{2}\left(\sigma_{22+}(\omega,v_z)\,\frac{I_+(i,\omega,n)}{\hbar\omega}+\sigma_{22-}(\omega,v_z)\,\frac{I_-(i,\omega,n+1)}{\hbar\omega}\right)$$

$$-\frac{n_{e2}^{\text{out}}(i,\omega,v_z,n)}{\tau}+\{[1-\theta(i)]n_{e2}^{\text{out}}(i-1,\omega,v_z,n)+\theta(i)n_{e2}^{\text{in}}(i,\omega,v_z,n)-n_{e2}^{\text{out}}(i,\omega,v_z,n)\}\frac{1}{T(i)},\tag{A1d}$$

$$\dot{n}_{g1}^{\text{in}}(i,\omega,v_z,n)=-\left[n_{g1}^{\text{in}}(i,\omega,v_z,n)-n_{e1}^{\text{in}}(i,\omega,v_z,n)\right]\frac{1}{6}\left(\sigma_{11+}(\omega,v_z)\,\frac{I_+(i,\omega,n)}{\hbar\omega}+\sigma_{11-}(\omega,v_z)\,\frac{I_-(i,\omega,n+1)}{\hbar\omega}\right)$$

$$-\left(n_{g1}^{\text{in}}(i,\omega,v_z,n)-\frac{3}{5}\,n_{e2}^{\text{in}}(i,\omega,v_z,n)\right)\frac{5}{6}\left(\sigma_{12+}(\omega,v_z)\,\frac{I_+(i,\omega,n)}{\hbar\omega}+\sigma_{12-}(\omega,v_z)\,\frac{I_-(i,\omega,n+1)}{\hbar\omega}\right)$$

$$+A_{11}n_{e1}^{\text{in}}(i,\omega,v_z,n)+A_{12}n_{e2}^{\text{in}}(i,\omega,v_z,n)+\left[n_{g1}^{\text{in}}(i+1,\omega,v_z,n)-n_{g1}^{\text{in}}(i,\omega,v_z,n)\right]\frac{1}{T(i)},\tag{A1e}$$

$$\dot{n}_{g2}^{\text{in}}(i,\omega,v_z,n)=-\left(n_{g2}^{\text{in}}(i,\omega,v_z,n)-\frac{3}{5}\,n_{e1}^{\text{in}}(i,\omega,v_z,n)\right)\frac{1}{2}\left(\sigma_{21+}(\omega,v_z)\,\frac{I_+(i,\omega,n)}{\hbar\omega}+\sigma_{21-}(\omega,v_z)\,\frac{I_-(i,\omega,n+1)}{\hbar\omega}\right)$$

$$-\left[n_{g2}^{\text{in}}(i,\omega,v_z,n)-n_{e2}^{\text{in}}(i,\omega,v_z,n)\right]\frac{1}{2}\left(\sigma_{22+}(\omega,v_z)\,\frac{I_+(i,\omega,n)}{\hbar\omega}+\sigma_{22-}(\omega,v_z)\,\frac{I_-(i,\omega,n+1)}{\hbar\omega}\right)$$

$$+A_{21}n_{e1}^{\text{in}}(i,\omega,v_z,n)+A_{22}n_{e2}^{\text{in}}(i,\omega,v_z,n)+\left[n_{g2}^{\text{in}}(i+1,\omega,v_z,n)-n_{g2}^{\text{in}}(i,\omega,v_z,n)\right]\frac{1}{T(i)},\tag{A1f}$$

$$\dot{n}_{g1}^{\text{out}}(i,\omega,v_z,n)=-\left[n_{g1}^{\text{out}}(i,\omega,v_z,n)-n_{e1}^{\text{out}}(i,\omega,v_z,n)\right]\frac{1}{6}\left(\sigma_{11+}(\omega,v_z)\,\frac{I_+(i,\omega,n)}{\hbar\omega}+\sigma_{11-}(\omega,v_z)\,\frac{I_-(i,\omega,n+1)}{\hbar\omega}\right)$$

$$-\left(n_{g1}^{\text{out}}(i,\omega,v_z,n)-\frac{3}{5}\,n_{e2}^{\text{out}}(i,\omega,v_z,n)\right)\frac{5}{6}\left(\sigma_{12+}(\omega,v_z)\,\frac{I_+(i,\omega,n)}{\hbar\omega}+\sigma_{12-}(\omega,v_z)\,\frac{I_-(i,\omega,n+1)}{\hbar\omega}\right)$$

$$+A_{11}n_{e1}^{\text{out}}(i,\omega,v_z,n)+A_{12}n_{e2}^{\text{out}}(i,\omega,v_z,n)+\{[1-\theta(i)]n_{g1}^{\text{out}}(i-1,\omega,v_z,n)+\theta(i)n_{g1}^{\text{int}}(i,\omega,v_z,n)$$

$$-n_{g1}^{\text{out}}(i,\omega,v_z,n)\}\frac{1}{T(i)},\tag{A1g}$$

$$\dot{n}_{g2}^{\text{out}}(i,\omega,v_z,n) = -\left(n_{g2}^{\text{out}}(i,\omega,v_z,n) - \frac{3}{5}\,n_{e1}^{\text{out}}(i,\omega,v_z,n)\right)\frac{1}{2}\left(\sigma_{21+}(\omega,v_z)\,\frac{I_+(i,\omega,n)}{\hbar\omega} + \sigma_{21-}(\omega,v_z)\,\frac{I_-(i,\omega,n+1)}{\hbar\omega}\right)$$

$$-\,[\,n_{g2}^{\text{out}}(i,\omega,v_z,n) - n_{e2}^{\text{out}}(i,\omega,v_z,n)\,]\,\frac{1}{2}\left(\sigma_{22+}(\omega,v_z)\,\frac{I_+(i,\omega,n)}{\hbar\omega} + \sigma_{22-}(\omega,v_z)\,\frac{I_-(i,\omega,n+1)}{\hbar\omega}\right)$$

$$+\,A_{21}n_{e1}^{\text{out}}(i,\omega,v_z,n) + A_{22}n_{e2}^{\text{out}}(i,\omega,v_z,n) + \{[\,1-\theta(i)\,]n_{g2}^{\text{out}}(i-1,\omega,v_z,n) + \theta(i)n_{g2}^{\text{in}}(i,\omega,v_z,n)$$

$$-\,n_{g2}^{\text{out}}(i,\omega,v_z,n)\}\,\frac{1}{T(i)}. \tag{A1h}$$

Further the cross sections are defined as

$$\sigma_{lk+} = \frac{\sigma_0}{1+[\,\delta+\xi+(-1)^l 0.5\zeta_g - (-1)^k 0.5\zeta_e\,]^2} \tag{A2}$$

and σ_{lk-} is described by analogous expressions but with a negative sign in front of v_z.

$$\xi = -\,\frac{\nu_0 v_z/c}{\Delta\nu_N/2}, \tag{A3a}$$

$$\zeta_g = \frac{\nu_g}{\Delta\nu_N/2}, \tag{A3b}$$

$$\zeta_e = \frac{\nu_e}{\Delta\nu_N/2}, \tag{A3c}$$

$$\delta = \frac{\nu-\nu_0}{\Delta\nu_N/2}. \tag{A3d}$$

ξ is a normalized Doppler shift and δ is a normalized laser detuning relative to the crossover line center, σ_0 is the cross section at resonance, $\Delta\nu_N$ is the natural linewidth (FWHM), ν_0 is the resonance frequency, ν_g is the splitting of the ground state, ν_e is the splitting of the excited state, c is the speed of light.

ACKNOWLEDGMENTS

[1] S. Svanberg, G.-Y. Yan, T. P. Duffey, and A. L. Schawlow, Opt. Lett. **11**, 138 (1986).
[2] S. Svanberg, G.-Y. Yan, T. P. Duffey, W.-M. Du, T. W. Hänsch, and A. L. Schawlow, J. Opt. Soc. Am. **4**, 462 (1987).
[3] C. Schmidt-Iglesias, L. Roso, and R. Corbalán, Opt. Lett. **15**, 63 (1990).
[4] O. Di Lorenzo-Filho, P. C. de Oliveira, and J. R. Rios Leite, Opt. Lett. **16**, 1768 (1991).
[5] C. Schmidt-Iglesias, L. Roso, and R. Corbalán, Opt. Commun. **90**, 251 (1992).
[6] C. Schmidt-Iglesias, R. Corbalán, and L. Roso, Opt. Commun. **98**, 72 (1993).
[7] Jiang Zhankui, A. Persson, L. Sturesson, and S. Svanberg, Z. Phys. D **21**, 315 (1991).
[8] H. Rinneberg, T. Huhle, E. Matthias, and A. Timmermann, Z. Phys. A **295**, 17 (1980).
[9] Luo Caiyan and S. Kröll (unpublished).
[10] A. Nottelmann, C. Peters, and W. Lange, Phys. Rev. Lett. **70**, 1783 (1993).
[11] D. Suter, Phys. Rev. A **46**, 344 (1992).
[12] D. Suter, M. Rosatzin, and J. Mlynek, Phys. Rev. A **41**, 1634 (1990).
[13] W. R. Bennett, Jr., Phys. Rev. **126**, 580 (1962).
[14] W. M. Fairbank, Jr., T. W. Hänsch, and A. L. Schawlow, J. Opt. Soc. Am. **65**, 199 (1975).
[15] J. E. Bjorkholm and A. Ashkin, Phys. Rev. Lett. **32**, 129 (1974).
[16] E. U. Condon and G. H. Shortley, *The Theory of Atomic Spectra* (Cambridge University Press, New York, 1959), p. 241.